Electronic Supplementary Information

Electrically and Magnetically Readable Memory with Graphene/1T-$CrTe_2$ Heterostructure: Anomalous Hall Transistor

Surabhi Menon and Umesh V. Waghmare

Theoretical Sciences Unit, Jawaharlal Nehru Centre for Advanced Scientific Research, Bangalore- 560064, India.

Fig. S1 (a) shows crystal structure of monolayer 1T-$CrTe_2$, where the brown and blue color spheres correspond to Te and Cr atoms respectively. With increase in the Hubbard U parameter the lattice constant varies linearly till U = 3 eV (see Fig. S1(b)). Lattice constant of monolayer 1T-$CrTe_2$ with U = 3 eV is 3.73 Å, which is consistent with earlier reported value. In the spin-polarized electronic structure along with partial density of states (PDOS), the spin-up conduction bands are significantly affected with inclusion of Hubbard U parameter of 2 eV (see Fig. S1(c) and (d)). This shows that inclusion of Hubbard U parameter in the calculations of electronic properties is crucial. Work function is the minimum amount of energy required to eject an electron from a system to infinity: W=V_{vac}-E_F, where V_{vac} is average potential energy in the vacuum and E_F is the Fermi energy. Work functions of graphene, monolayered 1T-$CrTe_2$, and the heterostructure estimated from planar and macroscopic average potentials, as shown in Fig. 2(c), are 4.26 eV, 5.35 eV, and 5.1 eV respectively (see Fig. S3(a) and Fig. S4(a)). When two layers with different work functions are in contact with each other, electrons redistribute between the layers to equalize the E_F. Visualization of m($\vec{r}$) (Fig. 3(b)) shows that Cr atoms contribute primarily to ferromagnetism of the heterostructure with estimated magnetic moment of +3.11 μ/atom, which is in good agreement with the theoretical estimate of +3 μ/atom reported in ML 1T-$CrTe_2$. Each Te atom has a small negative magnetic moment of -0.23 μ/atom. Spin-resolved PDOS (see Fig. S4 (b), (c) and (d)) shows that for spin-up and spin-down bands, the states near the Fermi level have maximum contributions from Cr-d and Te-p orbitals. As the Cr atom is in octahedral coordination in $CrTe_2$, the 3d orbitals are split into (1) doubly degenerate e_g orbitals (d_z^2 and $d_{x^2-y^2}$) (2) triply degenerate t_{2g} orbitals (d_{xy}, d_{xz} and d_{yz}). In Fig. S5. (a), the spin-resolved electronic structure near Γ point shows that Dirac point pins to Fermi level when doped with 0.11 e- per one unit cell of graphene in the heterostructure. The splitting of spin up/down bands due to exchange field increases after carrier doping for both spin channels. Also, after electron doping, the heterostrucutre shows enhanced electron transfer from graphene to 1T-$CrTe_2$ layer (see Fig. S5 (b)). The macrosopic average of electrostatic potential of electron doped heterostructure of graphene/1T-$CrTe_2$ (see Fig. S5 (c)) show strengthening of polarization. In Fig. S6 (a) and (b), we show the variation of magnetization and polarization for hole and electron doping. As a result of electron and hole doping, the magnetization per cell varies linearly. On the other hand, polarization decreases modestly with hole doping and changes drastically with electron doping. Such variations show that there is a magnetoelectric coupling expected in heterostructure. Now we look at the effect of strain on the electronic and magnetic properties of the

heterostructure. From Fig. S6 (c) and (d), it can be concluded that the magnetization of the heterostructure changes from 10.69 μB per cell to 10.75 μB per cell linearly with stress, which indicates that the in-plane biaxial strain, assumed to be isotropic, can affect the magnetization in the heterostructure, consequently giving rise to a piezomagnetic effect. It is also interesting to observe that the polarization also changes linearly with stress. From the atomic orbital-resolved electronic structure of graphene/1T-$CrTe_2$ heterostructure (shown in Fig. S7), it is clear that spin-up and spin-down bands at the Dirac point have predominantly C-p_z character. Both spin-up and spin-down bands near the Fermi level have contributions from Cr-d_z^2 , Cr-$d_{x^2-y^2}$, Te-p_x and Te-py orbitals. The states near Fermi level in spin-down bands of heterostructure consists of contributions from Cr-$d_{x^2-y^2}$, Te-p_x and Te-p_y orbitals, with stronger contribution from Te-p orbitals than of Cr. To attain the most stable configuration, graphene layer is moved along x and y-directions by 0.33 and 0.66 crystal coordinates, and we find negligible differences in energies of structures after relaxation (see Fig. S6). The presence of spin-orbit coupling (SOC) can significantly affect the band structure of materials, particularly those with heavy elements. The electronic structures graphene/ 1T-$CrTe_2$ heterostructure (see Fig. S9 (a), (b)) show that by including spin orbit coupling, the degeneracy breaks and results in splitting of bands, prominently in the conduction bands at Γ point. The overall impact of inclusion of SOC on the linear Dirac bands of graphene near Γ point remains relatively insignificant as $\Delta E \sim 0.2$ meV (see Fig. S9 (e)). We have examined the effect of electric field on the $CrTe_2$ layer. In the electronic structure of graphene/1T-$CrTe_2$ heterostructure, under application of positive perpendicular electric field (see Fig. S14), the graphene Dirac points shift towards valence bands and for negative electric field the graphene Dirac points shift towards conduction bands. It is important to note that the $CrTe_2$ bands remain largely unaffected under application of perpendicular positive and negative electric field. Interestingly, spin flip occurs between Dirac points at Γ point under application of negative electric field of 0.26 V/$\mathring{A}$ (see Fig. S15 (d)). Thus, our study holds true at low temperatures. We have also visualized the difference in electron densities without and with electric field of 0.05 V/Å. The visualization of $\Delta\rho$ shows charge transfer with electron accumulation at Te atoms and depletion at carbon atoms of graphene. The charge transfer in the pristine heterostructure results in p-type carriers in graphene. When electric field of 0.05 V/Å is applied in the positive z-direction, resulting in more p-type character and is also in accordance with the shift of Dirac points towards the conduction bands.

To assess its feasibility in terms of realistic devices, we simulated a field effect

transistor (FET) setup [1] as implemented in the Quantum Espresso package. The length of the periodic cell is L in z-direction (Fig. S18 (a)). A 2D charged plate, representing a gate electrode, was positioned at z = 0.0195 L. To prevent the doped carriers from moving too close to the gate electrode, a dielectric potential barrier with a height of 1.5 Ry and a width of 0.175 L was employed. We have also included a dipole correction opposite-charged plates to eliminate the electrostatic interactions between repeated cells. A dipole correction of -1.99 V/$\mathring{A}$ is applied in the positive z-direction to account for the electronic (heterostructure) and monopole charges. Within the vacuum region, the electric field should be zero, while between the gate and the system it is non-zero. The planar and macroscopic averages of electrostatic potential (Fig. S18 (b)) indicate a finite slope in the vacuum region. In principle, vacuum region needs to be increased so that E = 0, to avoid any charge spilling in the vacuum. Fig. S18. (c) shows that the electronic charge density in the potential barrier region is nearly zero. The spin-resolved electronic structure shows shift of Dirac points of graphene to 0.05 eV above the Fermi level after half-electron doped in the heterostructure with FET setup (Fig. S19).

We have investigated the Curie temperature (T_c) by comparing the exchange coupling (J) of monolayer and graphene/1T-$CrTe_2$ heterostructure. The classical Heisenberg Hamiltonian can be described as,

$$H = -\sum_{ij} J_{ij} S_i S_j \tag{1}$$

where J is the exchange coupling between the spin S_i at i^{th} site. The exchange coupling J is expressed in terms of exchange energy (E_{ex}) as:

$$J = \frac{E_{ex}}{2zS}, \tag{2}$$

where $E_{ex} = E_{AFM} - E_{FM}$ is the exchange energy, z is the number of nearest neighbor Cr atoms. Estimates of the total energies of monolayer $CrTe_2$ and heterostructure are presented in table below:

System	$E_{FM}(meV)$	$E_{AFM}(meV)$
Graphene/1T-$CrTe_2$	0	25
Monolayer 1T-$CrTe_2$	0	21

Table 1. Total energies of FM and AFM states of graphene/1T-$CrTe_2$ heterostructure and monolayer 1T-$CrTe_2$ with FM ground states.

We have followed a general procedure of sawtooth potential as implemented in Quan-

tum Espresso package. The key computational parameters include 'edir', which determines the direction of the electric field, 'emaxpos', which specifies the position within the unit supercell, where the electric potential reaches its maximum; 'eopreg', which defines the region of the unit cell over where sawtooth potential decreases and 'eamp', which sets the amplitude of the applied electric field. Sharp variations in v(z) occurs in the vacuum region (see Fig. S19).

1 Computational Details

Calculations for electronic structures (see Fig. S7) were performed using Vienna Ab initio Simulation Package (VASP) [2] within the framework of density functional theory. The generalized gradient approximation (GGA) in the Perdew-Burke-Ernzerhof (PBE) [4] form was used for the exchange-correlation functional. The plane-wave basis set was used with a kinetic energy cutoff of 800 eV. A Monkhorst-Pack k-point mesh of $7 \times 7 \times 1$ was used for the heterostructure. The convergence criteria for energy and forces were set to 10^{-5} eV and 0.01 eV/Å, respectively. The Hubbard U parameter was included in the calculations with a value of 2 eV for Cr atoms. Spin-orbit coupling (SOC) was included in the calculations of monolayer 1T-$CrTe_2$ and graphene/1T-$CrTe_2$ heterostructure using fully relativistic Projector Augmented Wave (PAW) potentials [3]. Calculations of AHC is based on a dense grid of 500 x 500 x 1 k-points in the Brillouin zone. In structural relaxation, convergence threshold values on the total energy and force were 10^{-6} Ry and 10^{-5} Ry/Bohr, respectively.

References

[1] Thomas Brumme, Matteo Calandra, and Francesco Mauri. Electrochemical doping of few-layer zrncl from first principles: Electronic and structural properties in field-effect configuration. *Physical Review B*, 89(24):245406, 2014.

[2] Georg Kresse and Jürgen Furthmüller. Efficient iterative schemes for ab initio total-energy calculations using a plane-wave basis set. *Physical review B*, 54(16):11169, 1996.

[3] Georg Kresse and Daniel Joubert. From ultrasoft pseudopotentials to the projector augmented-wave method. *Physical review B*, 59(3):1758, 1999.

[4] John P Perdew, Kieron Burke, and Matthias Ernzerhof. Generalized gradient approximation made simple. *Physical review letters*, 77(18):3865, 1996.

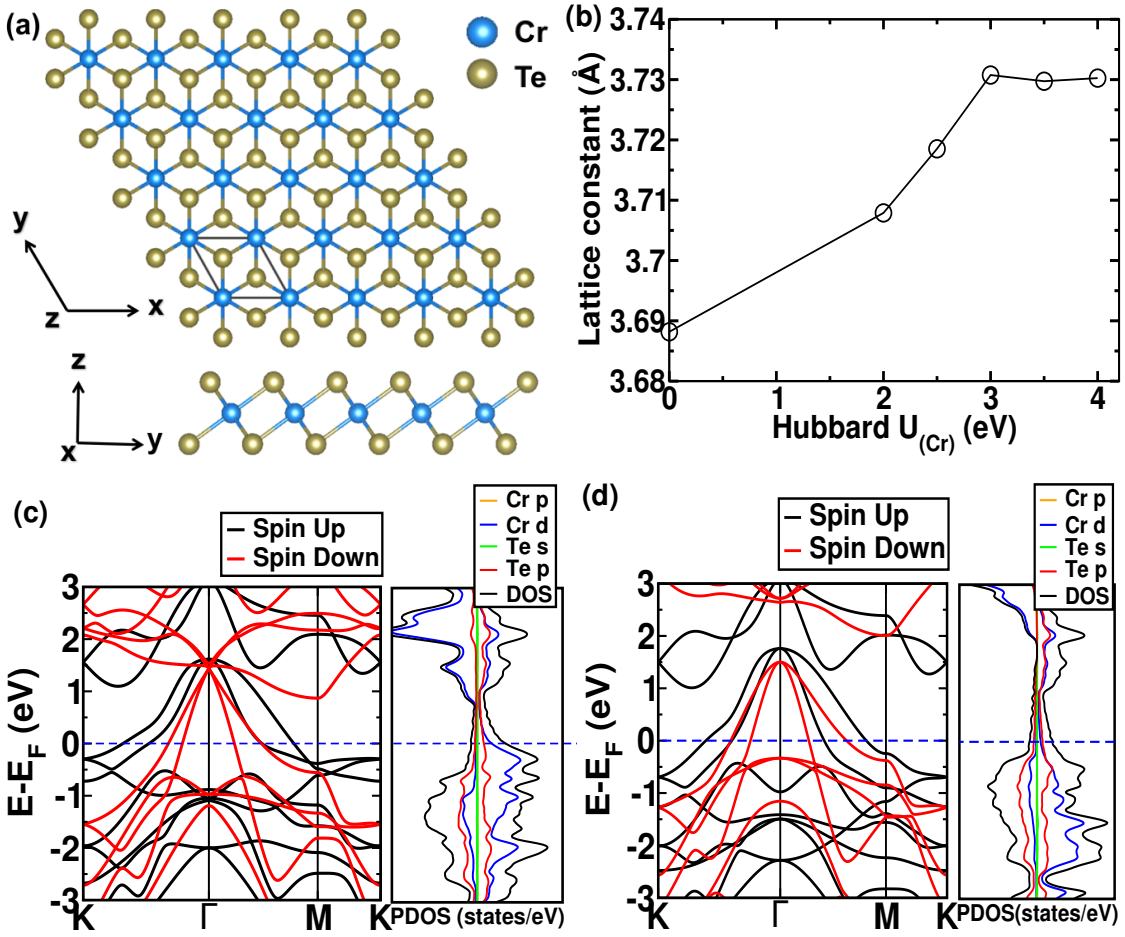

Fig. S1. (a) Top view and side view of crystal structure of monolayer of 1T-$CrTe_2$. The brown and blue balls represent Te and Cr atoms respectively. (b) Variation in lattice constant of structure with Hubbard U parameter. Calculated spin-polarized electronic structure of monolayer 1T-$CrTe_2$ along with partial density of states (PDOS) with Hubbard U (c) 0.0 eV and (d) 2.0 eV.

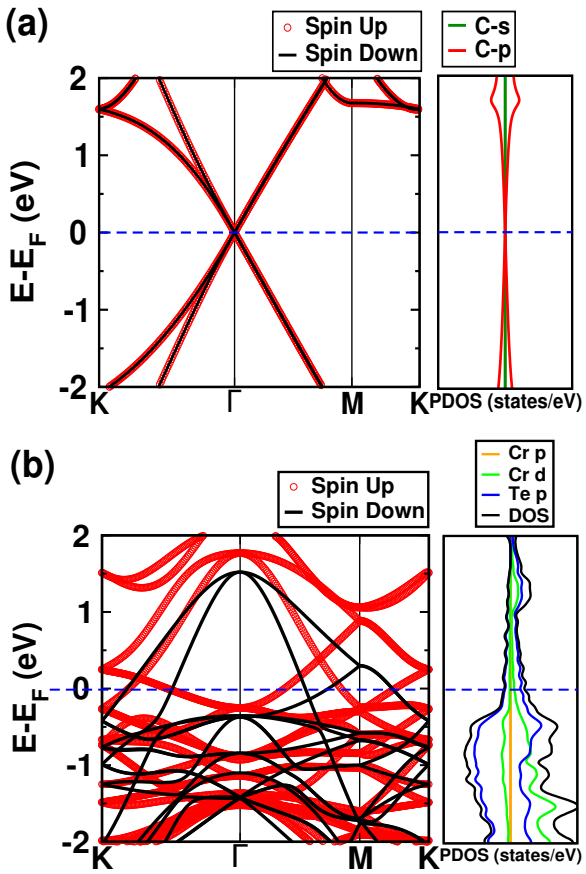

Fig. S2. Spin-resolved electronic structure (left) and projected density of states (right) of pristine graphene modelled with (3x3) periodic supercell (a) monolayered 1T-$CrTe_2$ modelled with (2x2) periodic supercell (b).

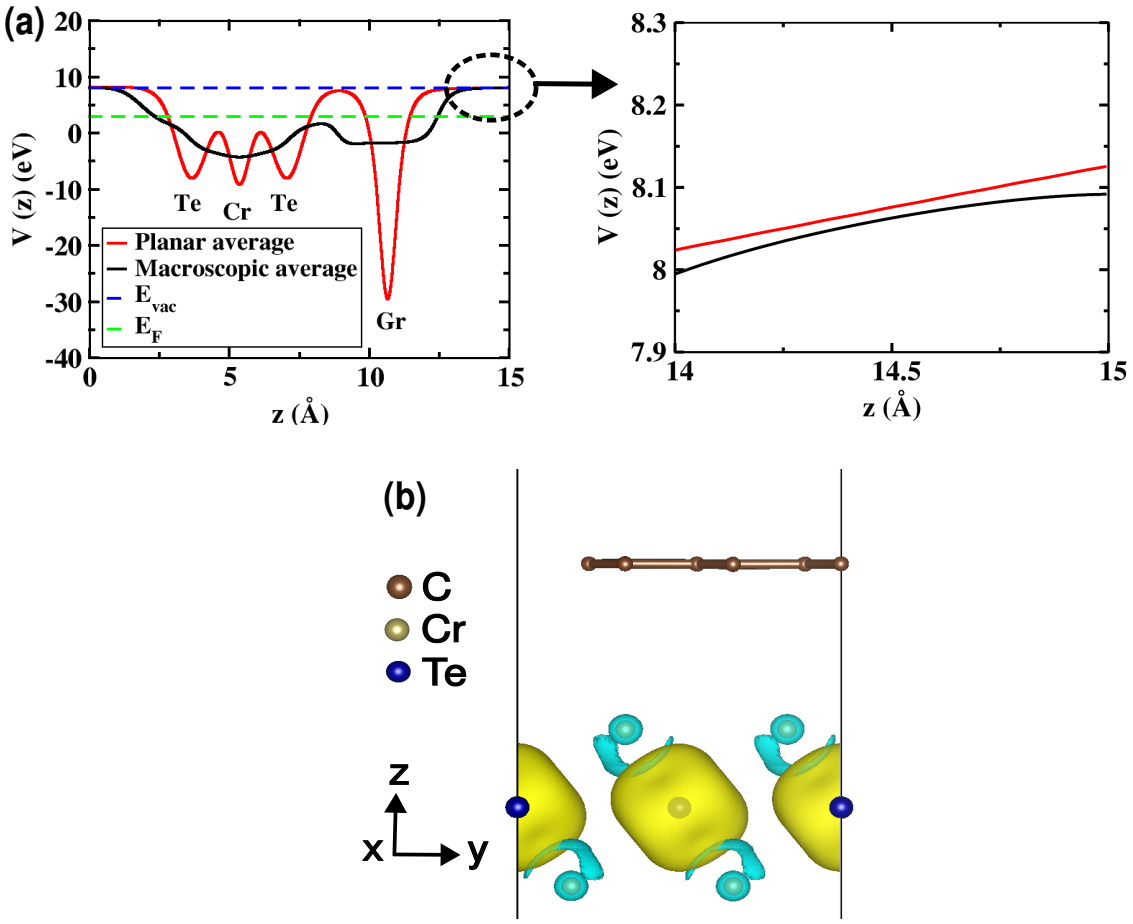

Fig. S3. Planar and macroscopic averages of electrostatic potential of graphene/1T-$CrTe_2$ heterostructure (a), and its nonzero slope in the vacuum (right panel) reveals its dipolar field and broken inversion symmetry. Isosurface of spin density of the heterostructure at isovalue of 0.006 e/Å^3 shown (b) with yellow and cyan colors showing positive and negative magnetization density on Cr and Te atoms respectively.

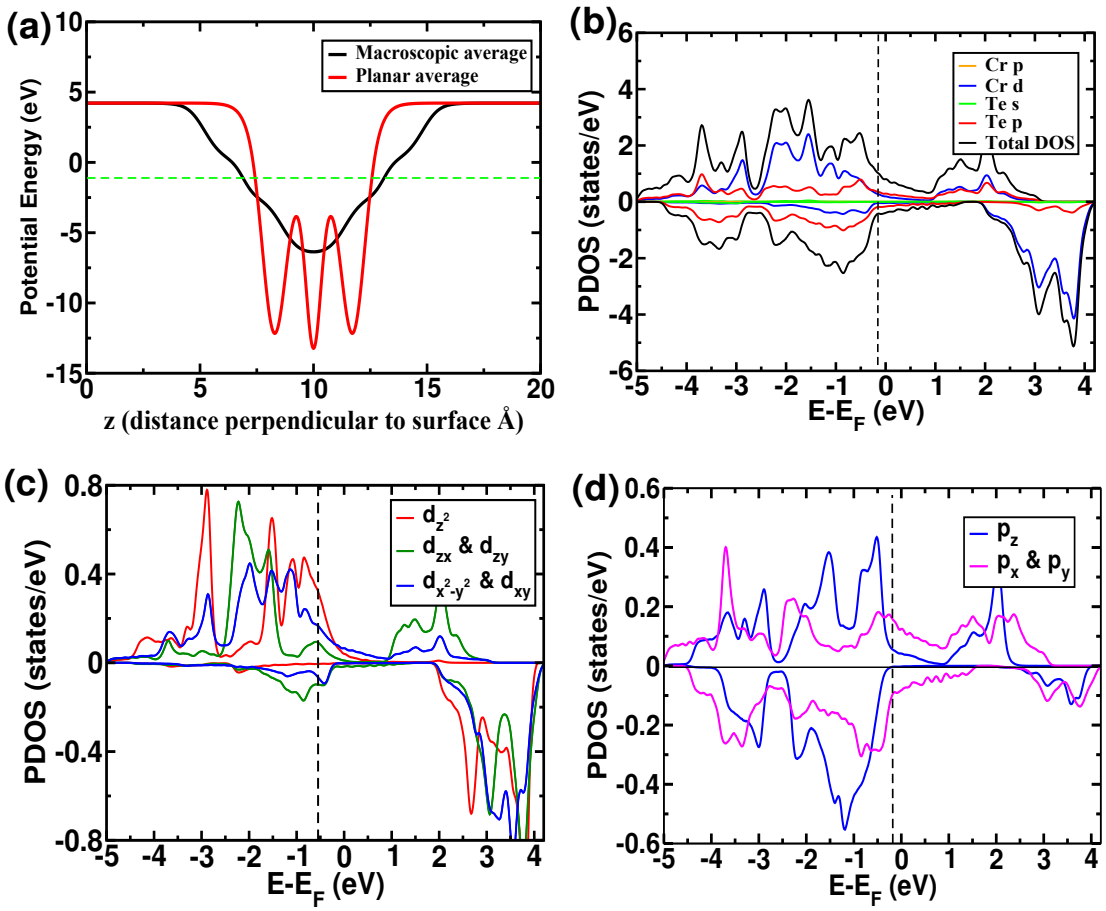

Fig. S4. (a) The macroscopic average and the average of the electrostatic potential for monolayer 1T-$CrTe_2$. Spin-resolved PDOS of (b) monolayer 1T-$CrTe_2$ (c) Cr-d orbitals (d) Te-p orbitals.

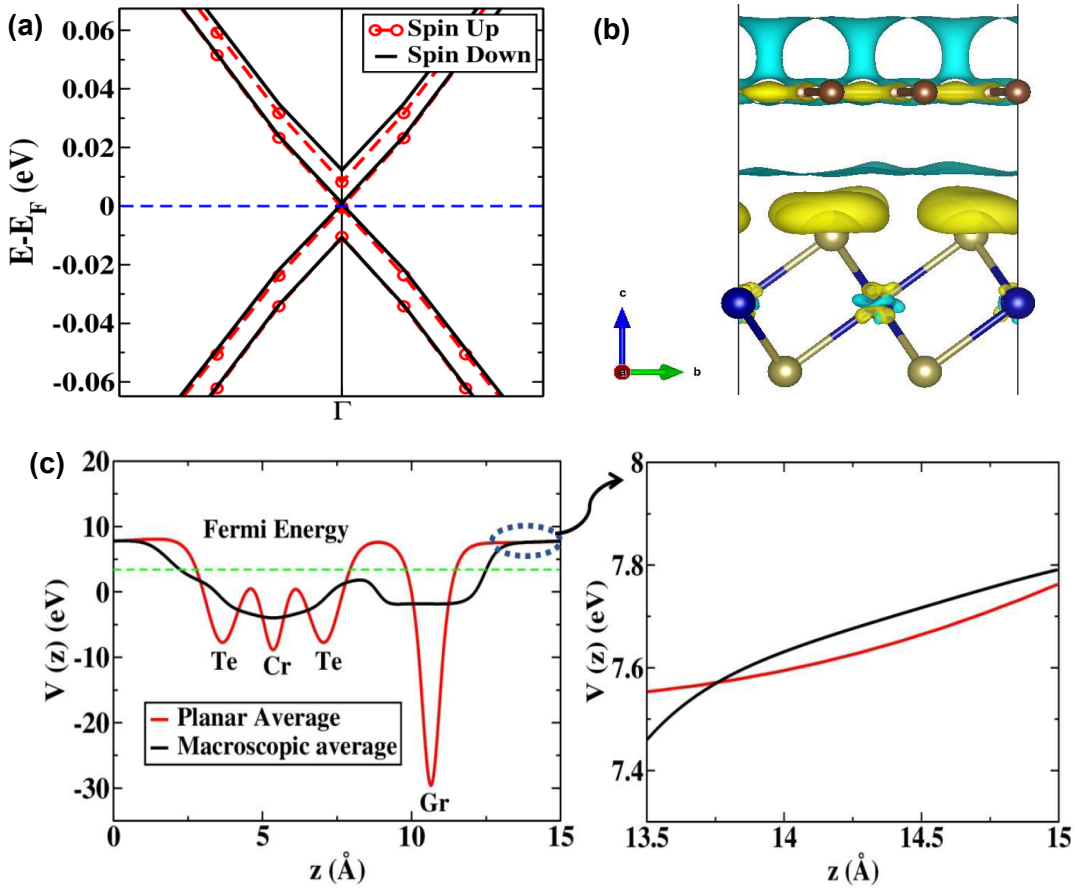

Fig. S5. (a) Enlarged electronic structure of one electron doped per two unit cells of heterostructure around Γ point. (b) Charge density difference with the isosurface value of 0.0001 e/Å^3. The cyan and yellow colors represent depletion and accumulation of electrons respectively. (c) Planar and macroscopic averages of electrostatic potential of electron doped heterostructure of graphene/1T-$CrTe_2$.

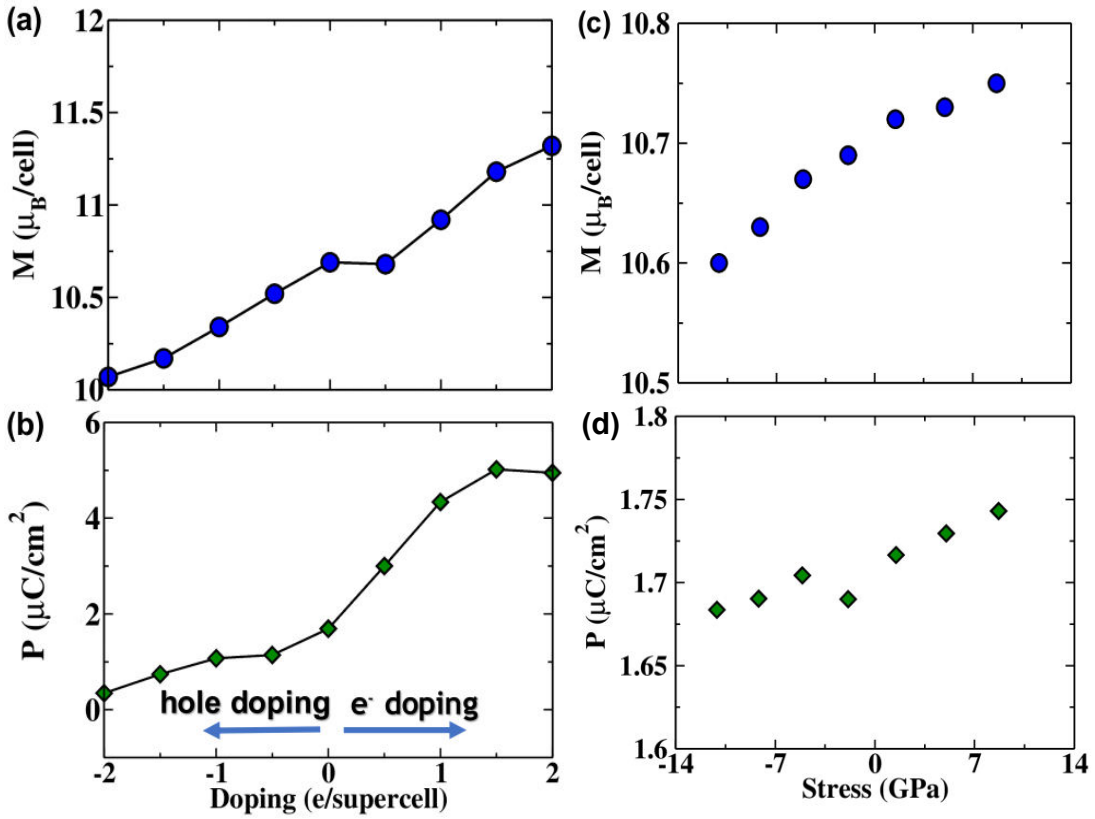

Fig. S6. Magnetization (M) and polarization (P) as a function of carrier doping (a), (b) and responses to corresponding biaxial stress (c), (d) in graphene/1T-$CrTe_2$ heterostructure.

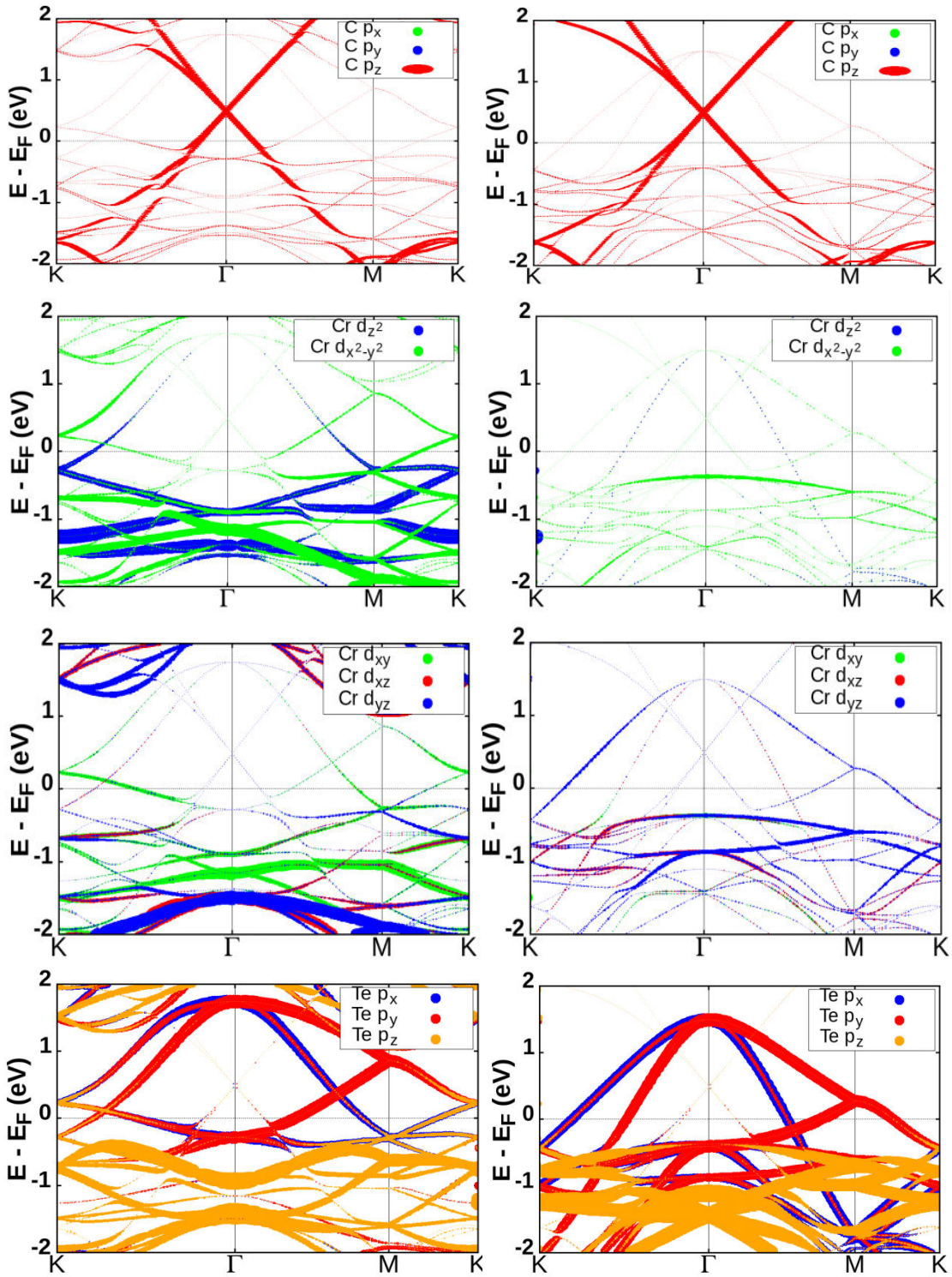

Fig. S7. Orbital-resolved electronic structure of graphene/1T-$CrTe_2$ heterostructure in spin-up (left) and spin-down (right) channels.

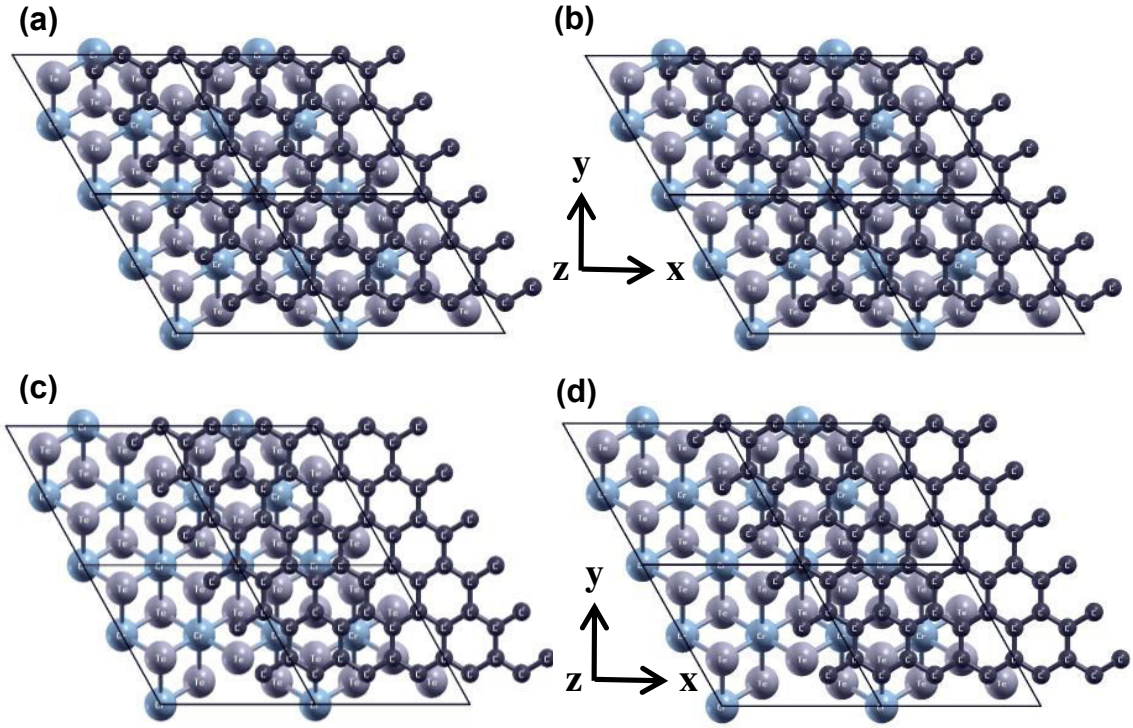

Fig. S8. Shift of graphene with respect to monolayer T-$CrTe_2$ by 0.33 and 0.66 crystal coordinates along x-direction. (a) and (c) before relaxation, and (b) and (d) after relaxation structures.

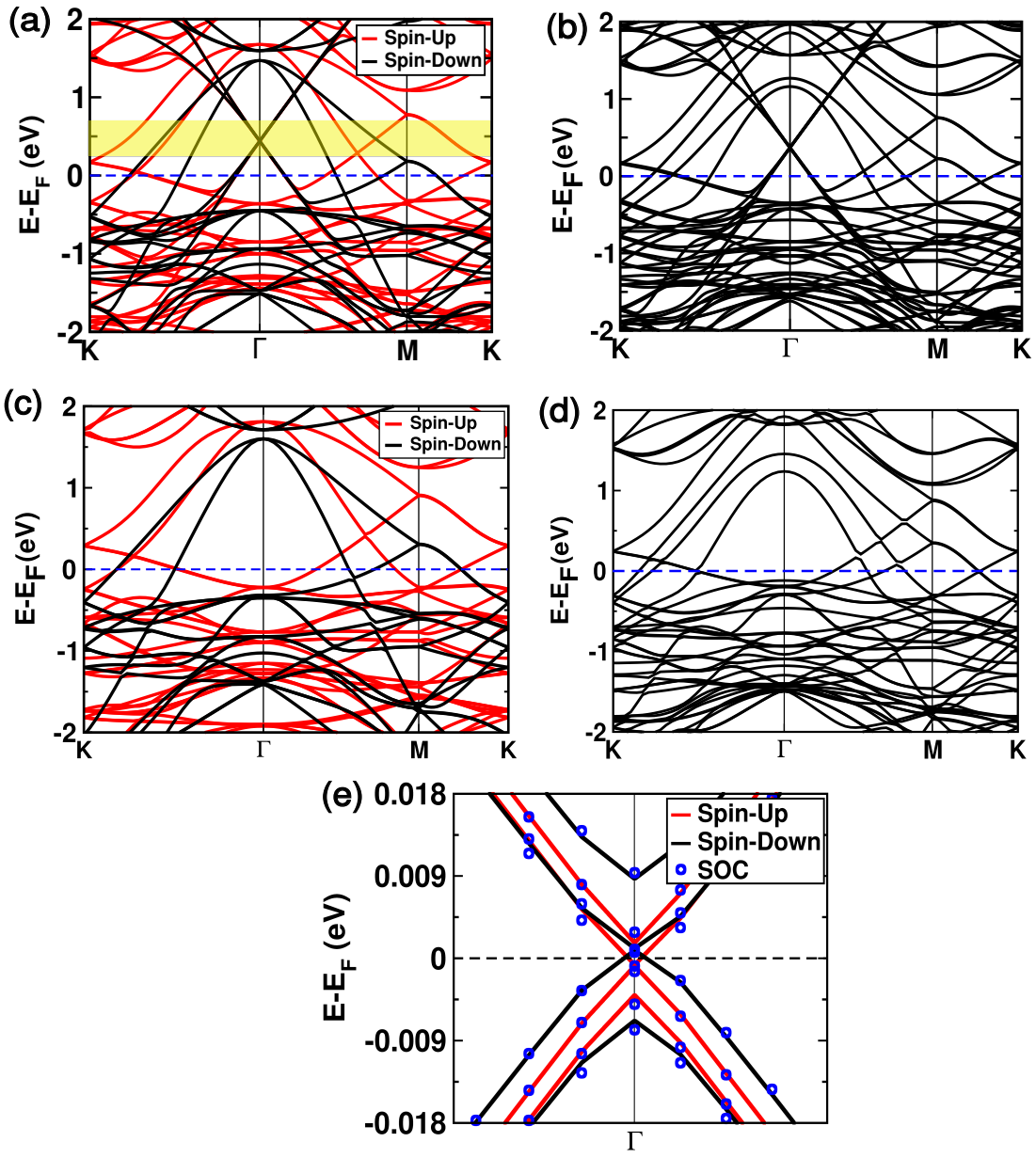

Fig. S9. Effect of spin-orbit coupling (SOC) on electronic structure of graphene/1T-$CrTe_2$ heterostructure. Electronic structure of graphene/1T-$CrTe_2$ heterostructure (a) without and (b) with SOC, monolayer 1T-$CrTe_2$ (c) and (d) without and with SOC, respectively. Electronic structures near Γ point of the heterostructure (e) with and without SOC, respectively obtained using VASP.

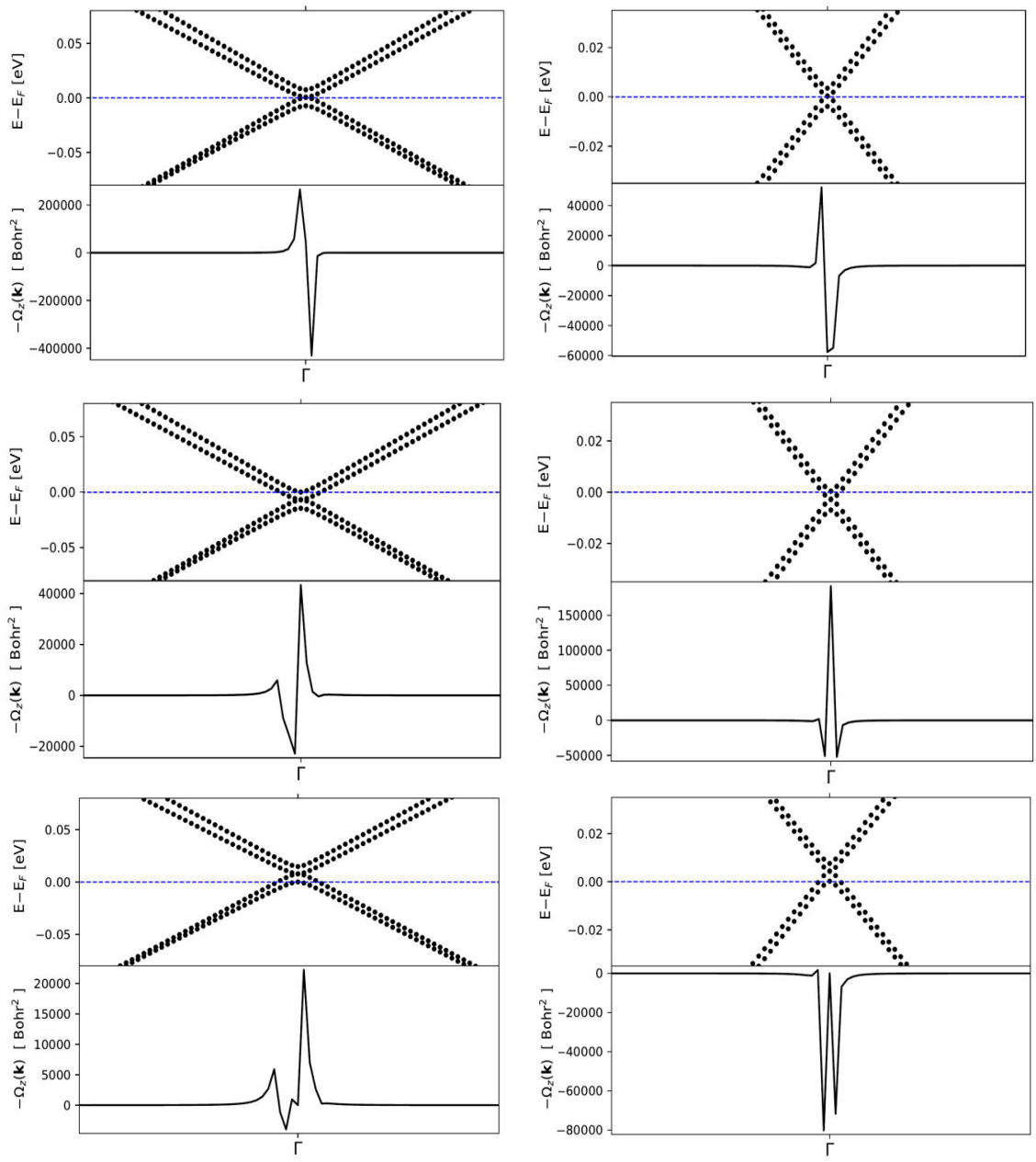

Fig. S10. Berry curvature of spin-up (left) and spin-down (right) bands near Γ point of graphene/1T-$CrTe_2$ heterostructure as a function of the Fermi level (E_F) obtained using Wannier90.

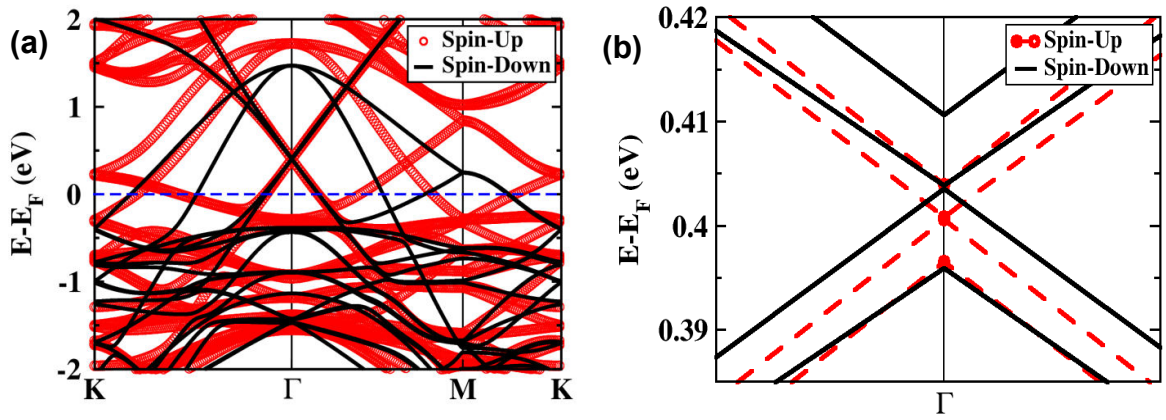

Fig. S11. Electronic structure of graphene/1T-$CrTe_2$ heterostructure using wannier90 for spin-up (left) and spin-down (right) channels.

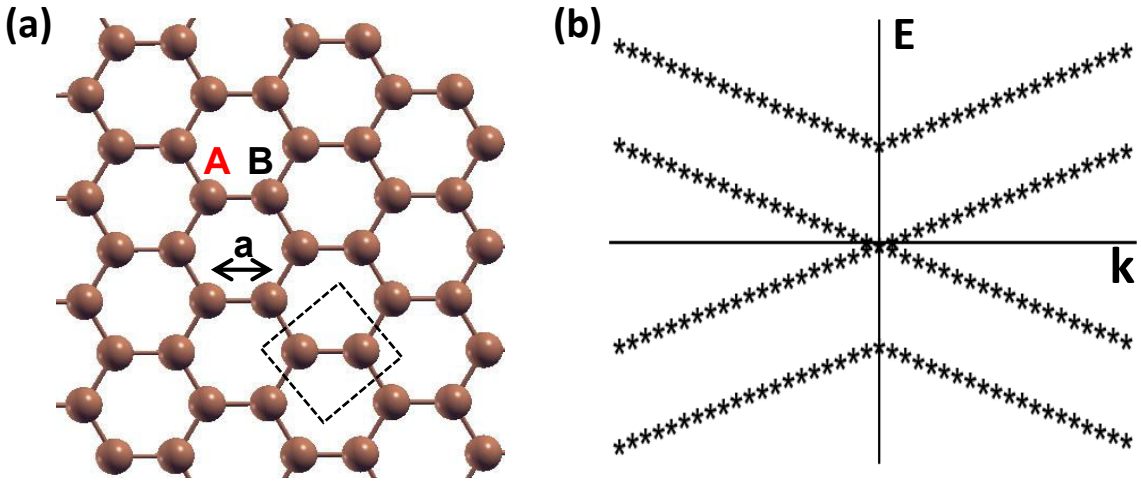

Fig. S12. Crystal structure of pristine graphene. Dispersion of electronic bands (spin-up) near the Dirac points at Γ point (b) obtained with a continuum model with crystal field parameter.

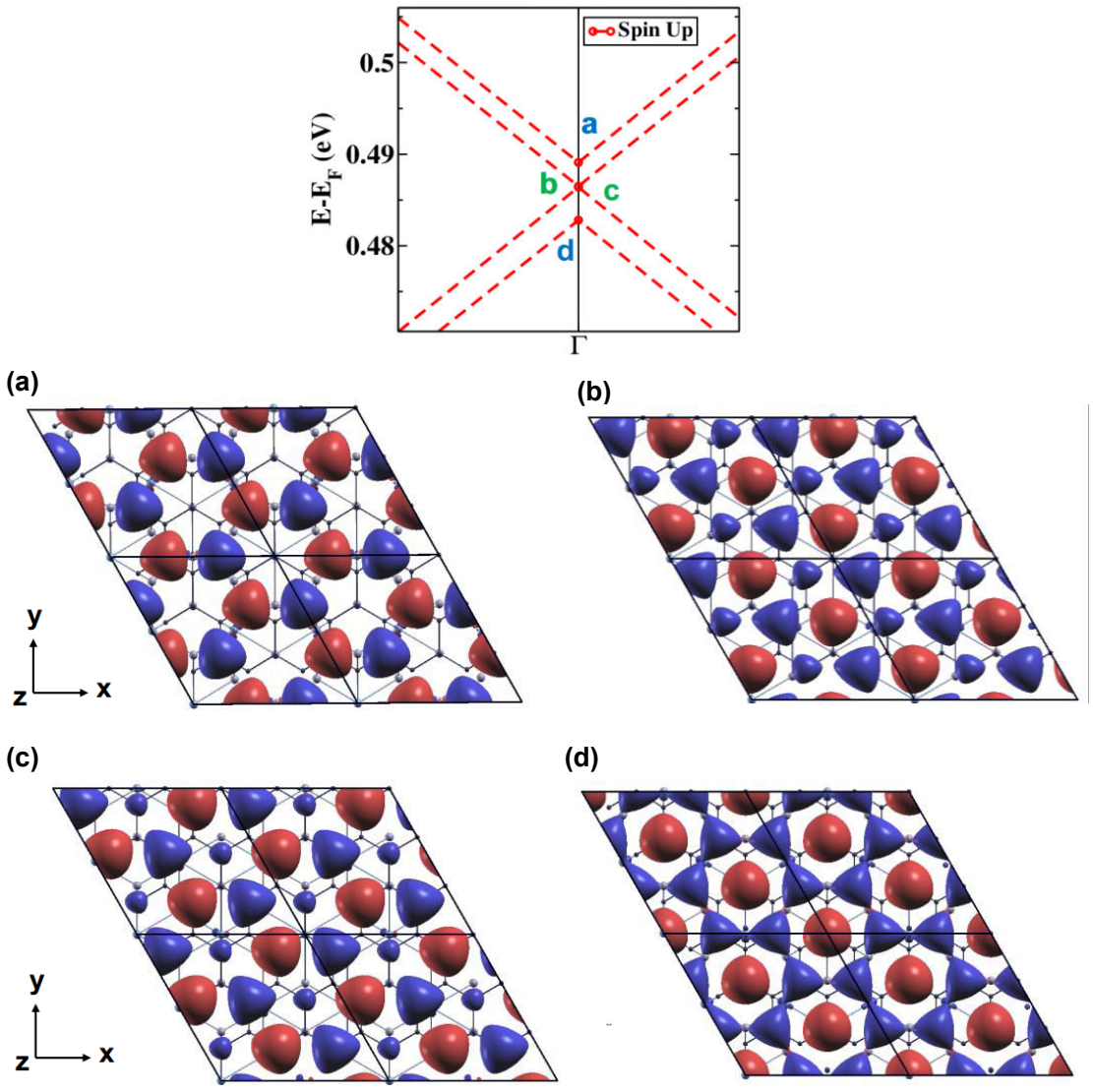

Fig. S13. Electronic structure of graphene/1T-$CrTe_2$ heterostructure and isosurfaces of wavefunctions of Dirac points for spin-up channel at Γ point for corresponding bands marked as a,b,c and d. The positive and negative isosurfaces are shown as red and blue, respectively.

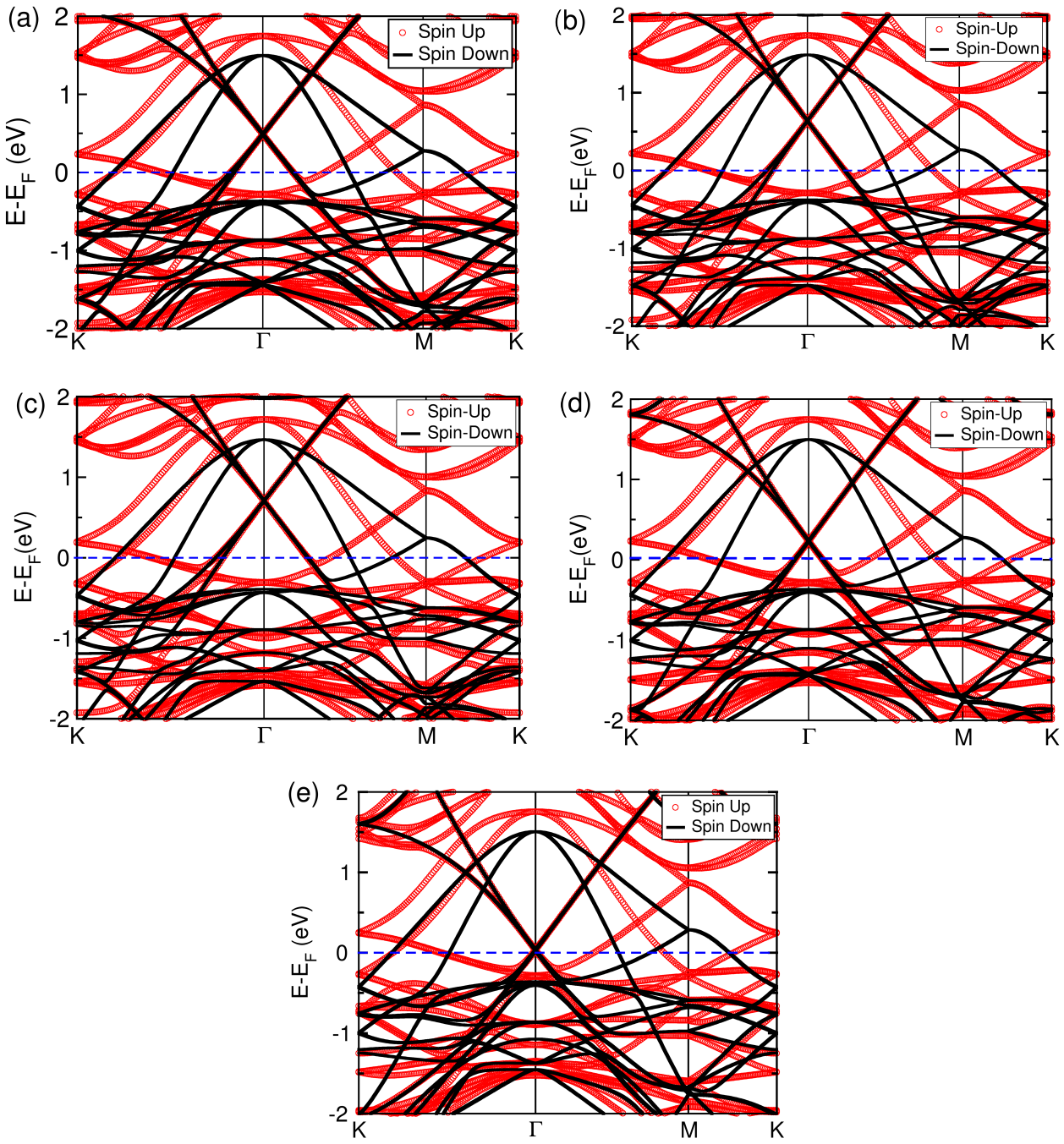

Fig. S14. Spin-resolved electronic structures of graphene/1T-$CrTe_2$ heterostructure at (a) E = 0 V/ Å (a) E = 0.1 V/Å (b) E = 0.26 V/Å (c) E = -0.1 V/Å and (d) E = -0.26 V/Å, modeled with sawtooth potential.

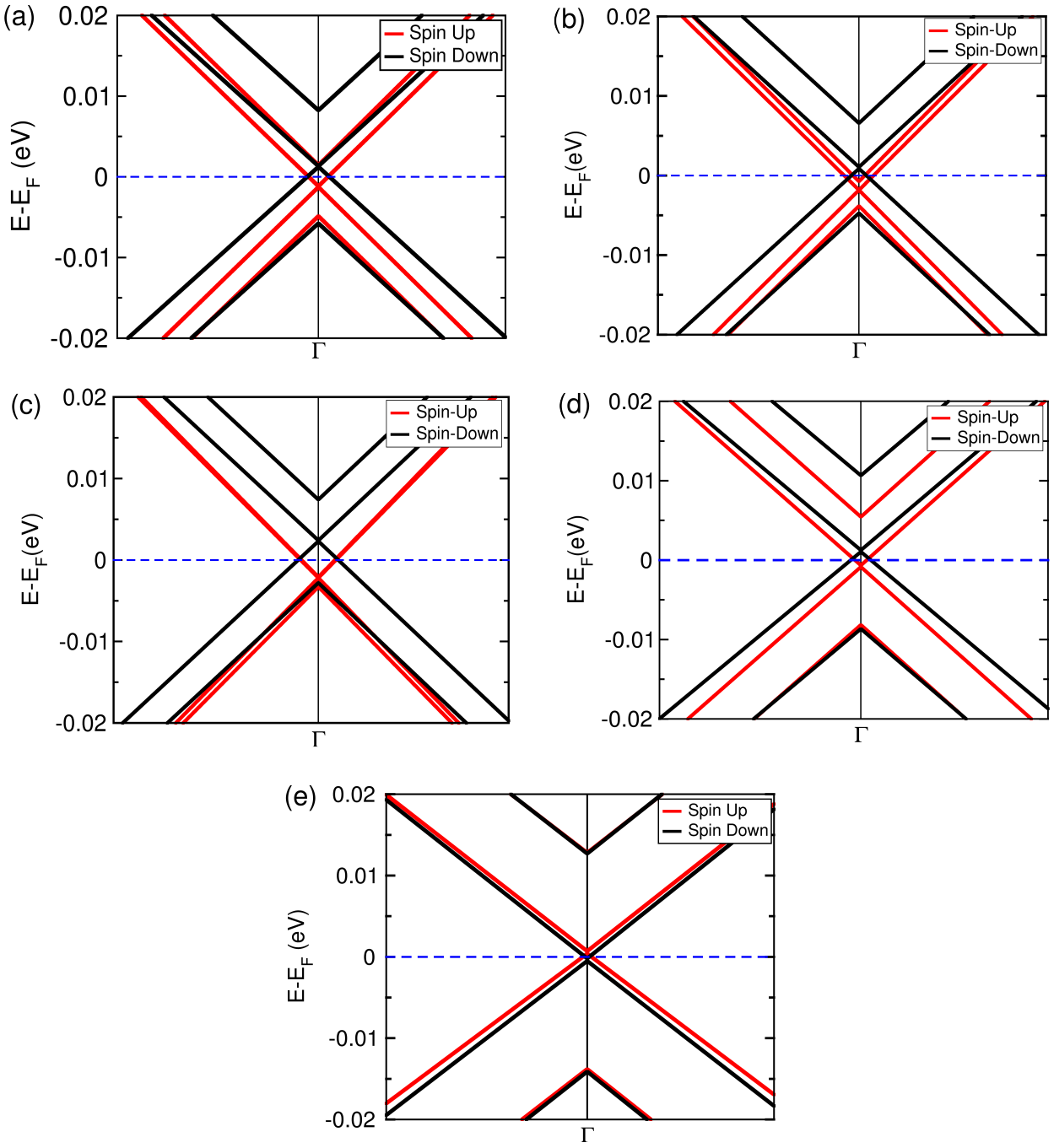

Fig. S15. Zoomed view of spin-resolved electronic structures in the vicinity of Dirac points of graphene/1T-$CrTe_2$ heterostructure at (a) E = 0 V/ Å (a) E = 0.1 V/Å (b) E = 0.26 V/Å (c) E = -0.1 V/Å and (d) E = -0.26 V/Å, modeled with sawtooth potential.

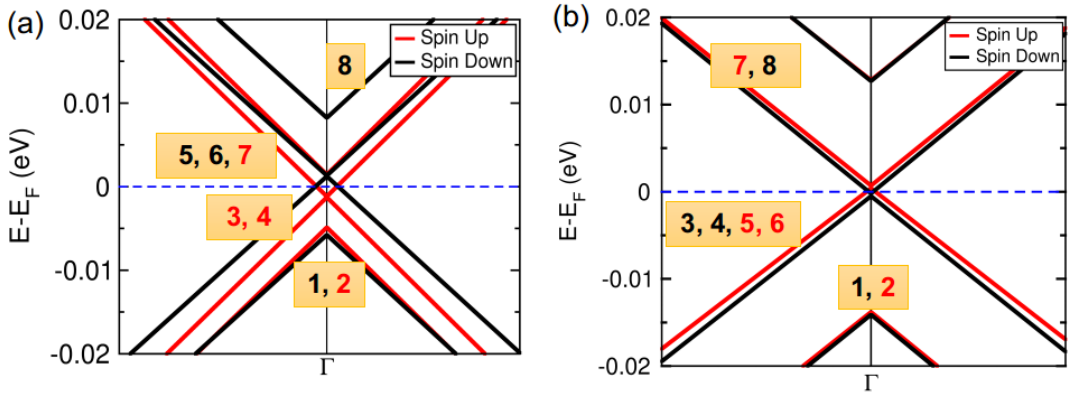

Band index	E - E_F (eV)	
	E = 0 V/Å	E = -0.26 V/Å
1	-0.0058 (↓)	-0.0141 (↓)
2	-0.0049 (↑)	-0.0138 (↑)
3	-0.0013 (↑)	-0.0005 (↓)
4	-0.0013 (↑)	-0.0002 (↓)
5	0.0012 (↓)	0.0004 (↑)
6	0.0013 (↓)	0.0007 (↑)
7	0.0014 (↑)	0.0126 (↑)
8	0.0082 (↓)	0.0128 (↓)

Fig. S16. Spin-resolved electronic structures of graphene/1T-$CrTe_2$ heterostructure near the Dirac points under application of (a) E = 0 V/Åand (b) E = -0.26 V/Å. Table showing comparison of energy eigenvalues of graphene bands near Γ point in the electronic structure of heterostructure under application of perpendicular electric field of -0.26 V/Å, modeled with sawtooth potential.

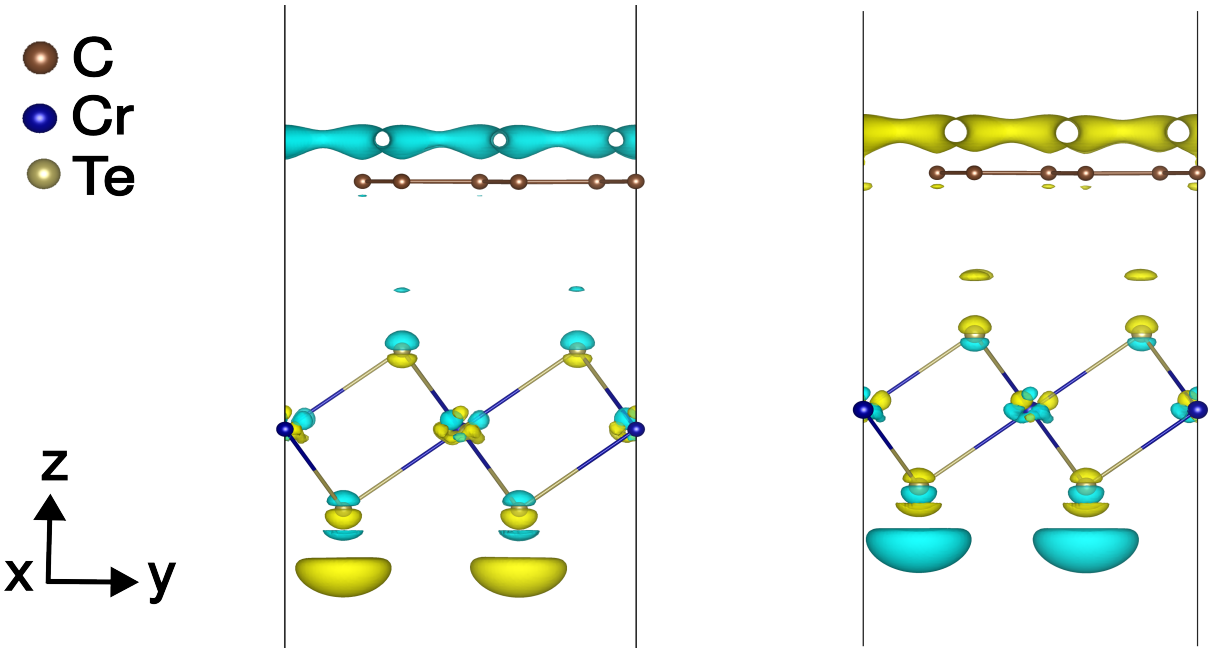

Fig. S17. Visualization of difference in electron densities with and without electric field (0.05 V/Å) with isosurface value of 0.00009 e/Å^3. The yellow and cyan color indicate the accumulation and depletion regions for electrons.

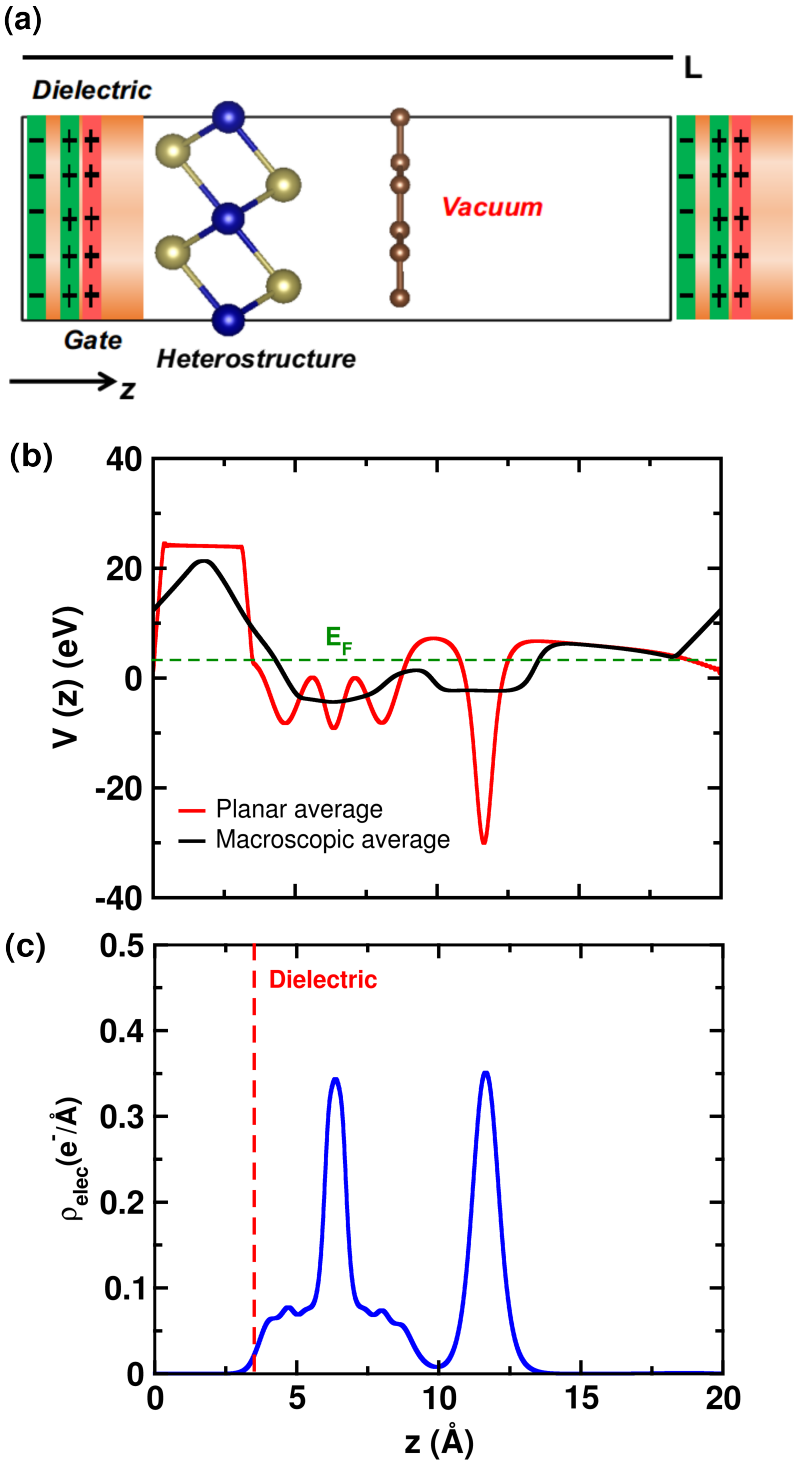

Fig. S18. (a) Schematic of an FET setup simulated using periodic boundary conditions, where the heterostructure is placed in front of a charged plane mimicking the metallic gate. The heterostructure is doped with half electron per unit supercell, such that the charged plane (in red color) is positively charged along with a dipole (in green color). We include a dielectric separation layer (in orange color) to separate the channel and its carriers from the gate plate. (b) Planar and macroscopic averages of the electrostatic potential and (c) planar average of electronic charge density of electron doped graphene/1T-$CrTe_2$ heterostructure.

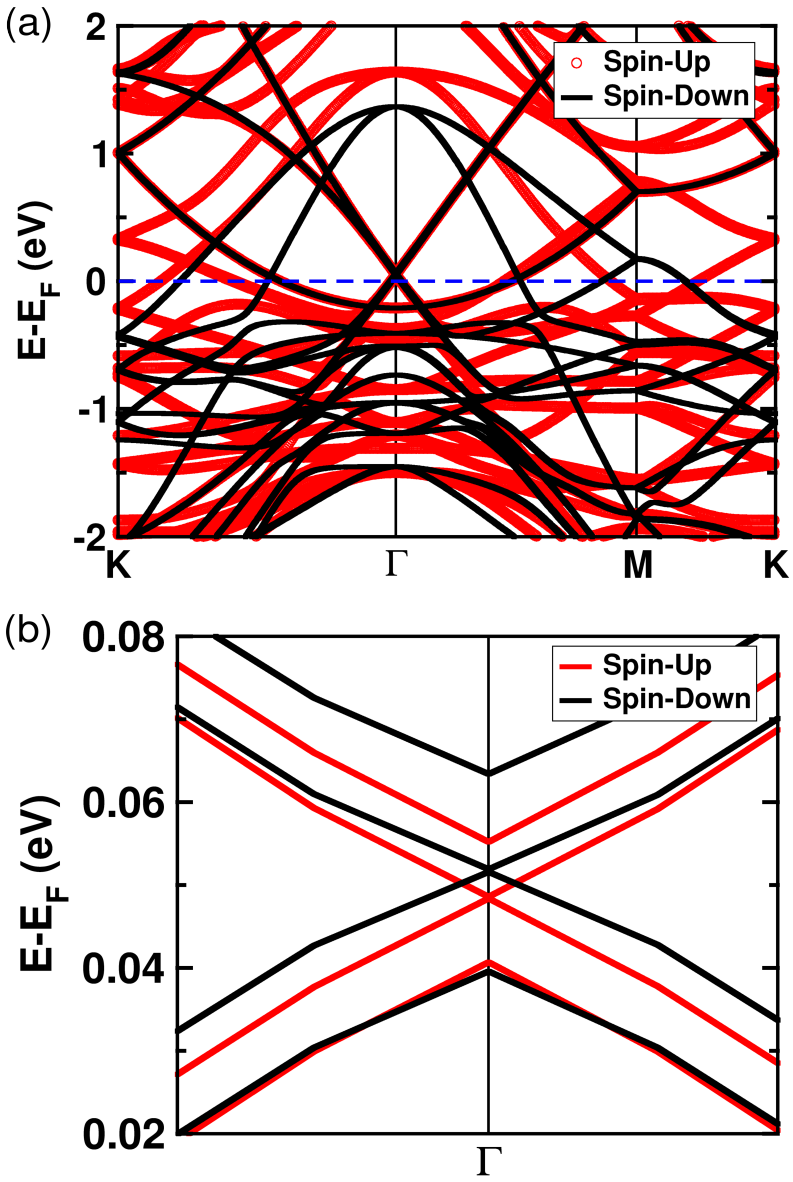

Fig. S19. (a) Spin-polarized electronic structure of gated graphene/1T-$CrTe_2$ heterostructure and (b) zoomed view of frontier bands near the Dirac points of graphene in the heterostructure placed in front of charged gate mimicking metallic gate. The Dirac points is $\sim$ 0.05 eV above the Fermi level.

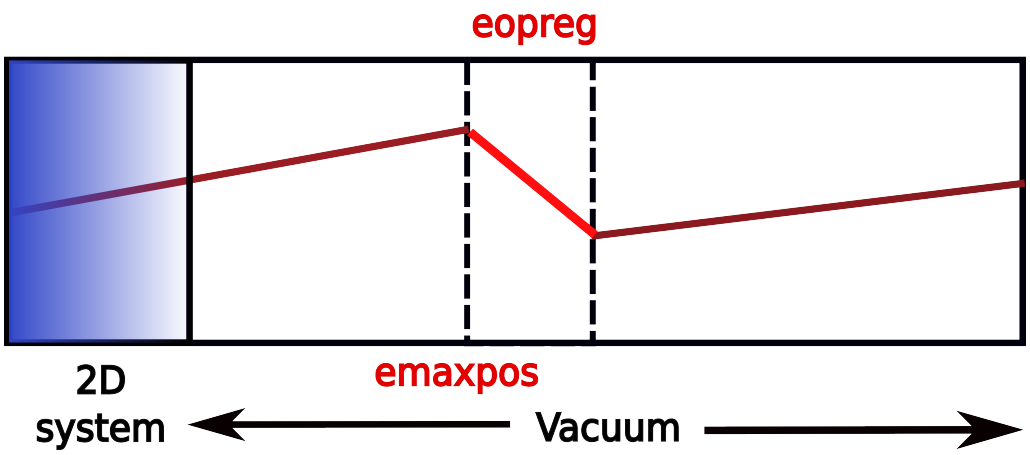

Fig. S20. Schematic showing procedure of implementation of sawtooth potential in a 2D system with vacuum.

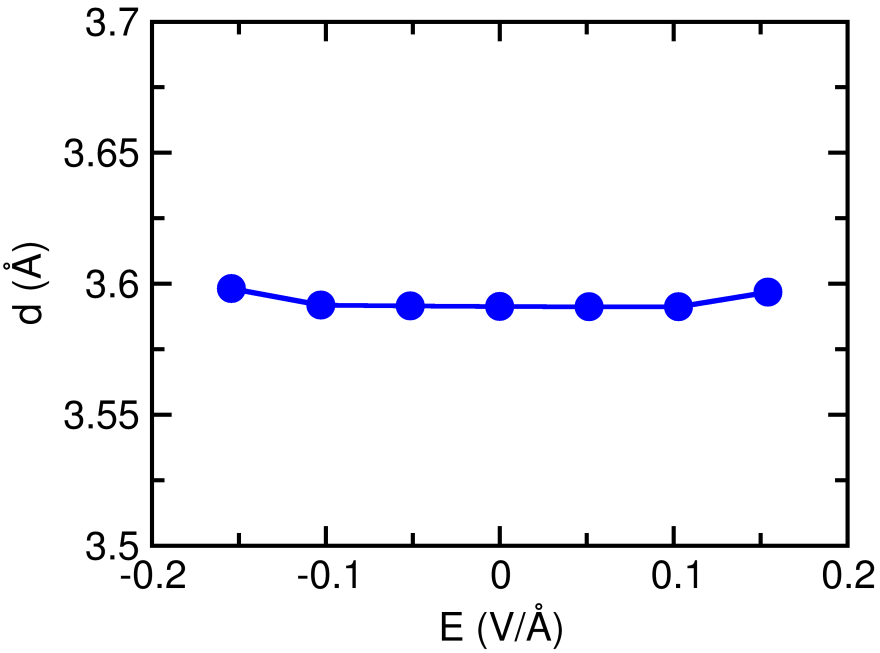

Fig. S21. Influence of external electric field on the interlayer distance (d) of graphene/1T-$CrTe_2$ heterostructure.